Evaluation Scheme for EMI of Train Body Voltage Fluctuation on the BCU Speed Sensor Measurement

Ke Huang, *Student Member, IEEE*, Zhigang Liu, *Senior Member, IEEE*,
Feng Zhu, Zongsheng Zheng, and Ye Cheng

Abstract—The voltage fluctuation between the train body (TB) and the train's wheel axis (TB voltage fluctuation for short), might cause electromagnetic interference (EMI) on brake control unit (BCU) speed sensor in some high-speed trains (HSTs), which may cause faulty measurement of train speed and incorrect operation of train door. Using a relevant event that occurred in China railways high-speed 380CL-type train as case study, this paper presents an evaluation scheme for the EMI influence of TB voltage fluctuation on the speed measurement of BCU speed sensor. First, the EMI channels are researched, and a model representing the relation between TB voltage and voltage signal reflecting measured speed is deduced. Second, an evaluation scheme for speed measurement influenced by EMI is designed on this basis, where TB voltage and voltage signal reflecting measured speed are taken as the input and the output of model, respectively. The evaluation aimed at EMI is realized by judging the correctness of model output. Later, a real-life experiment is performed in the Chinese Nanjing station to verify the validity and feasibility of evaluation scheme. Last, some application studies are made to evaluate the presented scheme under multiple specific conditions, such as different TB contact conditions or different train speeds. The comparison results illustrate that the scheme can not only provide an opportunity to judge the correctness of speed measurement under the premise of collecting TB voltages, but also provide references in taking timely measures to prevent faulty speed measurement such as weakening TB voltage fluctuations.

Index Terms—Brake control unit (BCU) speed sensor measurement, electromagnetic interference (EMI), evaluation scheme, high-speed train (HST), train body (TB) voltage fluctuation.

I. INTRODUCTION

CHINESE ac high-speed train (HST) systems have been developing rapidly, with a passenger capacity volume of 2315.6 million people using high-speed railway (HSR) during the Chinese New Year of 2016. The increasingly larger flow volume of passenger will bring bigger and bigger challenges to railway traffic. Despite the rapid development
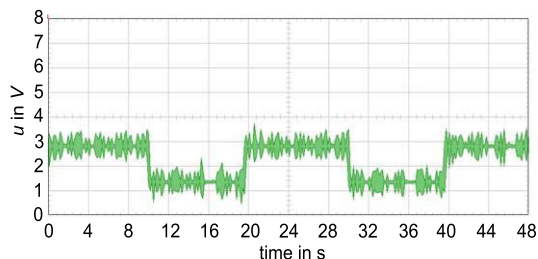
Fig. 1. Waveform of $u(t)$ when the faulty speed measurement occurred.

of HST, some problems about the electromagnetic interference (EMI) still exist in the train's operation, such as faulty speed measurement caused by EMI. Because, the brake control unit (BCU) sensor has high-measurement accuracy and excellent anti-interference ability toward vibration, pressure, temperature, etc., it is applied to some types of HST in German HSR and is generally adopted in Chinese HSR for speed measurement now. However, some EMI problems have not been completely solved in the usage of this sensor. Taking a relevant event that occurred in the China railways high-speed (CRH) 380CL-type train at the Chinese Wu-Xi railway station as an example [1], the door of the tenth train body (TB) could not open normally when the docked train was ready to run, which affects passengers to get on trains. The fault was found to be caused by the EMI on the BCU speed sensor, which may be related to the voltage fluctuation between the TB and the train's wheel axis (TB voltage fluctuation for short). For the BCU speed sensor, when the docked HST had been supplied with electric power and was ready to run, HST speed is 0 km/h and a dc signal with 15 V is expected for the signal input into the BCU speed sensor's control terminal [$u(t)$]. Nevertheless, according to on-site survey, the overall trend of the $u(t)$ presented a rectangular wave as depicted in Fig. 1. The measured speed based on the waveform of $u(t)$ was 6.3 km/h. As a result, the door refused to open in order to secure passengers safety as the door will only open when the measured speed is below 5 km/h. Therefore, further study of the EMI on the BCU speed sensor's measurement is necessary to ensure reliable operation of HST.

Focusing on the EMI problem of the sensor, many researchers have performed studies [2]–[6]. In [2], Creosteanu analyzed an aircraft engine speed sensor in terms of inductive coupling, and found that the EMI source is the induced voltage from the high current coil in the approaching wire. The

effect of EMI on the aircraft engine's speed sensor was also studied by experiment [3]. For the Hall-effect current sensor that is also used in the BCU speed sensor interior, Aiellio concluded that it is susceptible to EMI [4]. By analyzing the electromagnetic compatibility (EMC) in the displacement sensor source, S. Hussmann considered that pulse width modulation (PWM) is able to provide a pure source [5]. There are also some sensors designed for EMI assessment and suppression. S. Dhia presented an on-chip noise sensor to analyze circuit susceptibility to EMIs [6]. A new accurate and rapid EMC measurement method was proposed for the integrated circuit design of intelligent sensors [7]. The ironless inductive position sensor, which presents intrinsic immunity to external magnetic fields, was designed in [8] for location measurements in harsh environments. An analysis model of its working principle has been established and preliminarily verified in [9]. Nevertheless, because the EMI issue about a HST speed sensor has only caused concern of railway field recently and is a very new topic, corresponding studies are relatively few, currently. Work mainly focuses on the high-frequency electrical conditions. Combined with some experimental investigations, J. Yang concluded that the damage of sensor under pantograph-catenary detachment was caused by transient TB voltage fluctuation [10]. Additionally, the influencing mechanism of the TB voltage fluctuation on the speed sensor under HST's dropping pantograph was discussed and concluded as inductive coupling in [10] and [11].

Focusing on the TB voltage fluctuation problem, a large number of analyses on its generation mechanism, influencing factors, and suppression measures have been conducted, such as [12]–[16]. For example, as for different surge conditions, the causes of violent TB voltage fluctuation were studied from HST's grounding angle. It was concluded that the causes include the capacitive coupling of high-voltage cable on TB and the high- TB grounding impedance with the appearance of a surge [12]–[14]. On this basis, the nonlinear electrical characteristics aimed at some types of TB grounding devices were discussed [15]. Some scholars also studied the violent TB voltage fluctuation caused by lightning catenary [16].

As an extension of previous works, this paper presents an evaluation scheme aimed at the TB voltage fluctuation's EMI influence on the BCU speed sensor's speed measurement. The influential mechanism of TB voltage fluctuation is concluded, including not only inductive coupling, but also capacitive coupling. The scheme is applicable to low-frequency electrical conditions where only power-frequency (50 Hz in China) component and low-frequency components including some harmonics exist in train's voltages and currents. In Fig. 2, this scheme is based on an equation representing the relation between $u(t)$ (also named voltage signal reflecting measured speed) and TB voltage. The equation is also defined as an impact model of TB voltage fluctuation on speed measurement in this paper. The actual HST speed is set as inherent factor of this model. TB voltages and $u(t)$ are the input and the output of the model, respectively. The measured speed with the impact of TB voltage fluctuation (v) is then obtained according to the waveform of model output. Last, by comparing with the actual HST speed (v), the correctness of measured speed
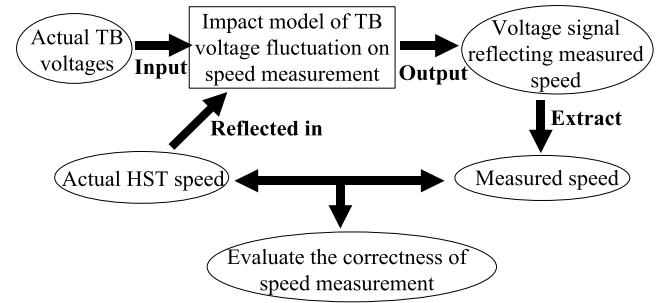

Fig. 2. Flowchart of the presented evaluation scheme.

TABLE I
SYMBOL MEANINGS

Symbol	Meaning
$u_{tb}(t)$	Voltage between the train body and the train's wheel axis
$u_v(t)$	Source voltage in BCU speed sensor
$u_L(t)$	Voltage of $R_L(t)$
$u_S(t)$	Voltage signal sent into BCU control terminal (without any interference)
$u(t)$	Actual voltage signal sent into BCU control terminal
$u_n(t)$	Interference voltage caused by $u_{tb}(t)$
$u_D(t)$	Voltage signal output by BCU control terminal

is judged. This evaluation scheme not only gives a chance to judge the correctness of speed measurement under the premise of collecting TB voltages, but also provides references in taking timely measures for preventing faulty speed measurement such as weakening TB voltage fluctuations.

The rest of this paper is organized as follows. The influence mechanism of the TB voltage fluctuation on the BCU speed sensor is discussed, and a model reflecting the relation between voltage signal reflecting measured speed and TB voltages is proposed in Section II. In Section III, based on this model, an evaluation scheme for the speed measurement with EMI impact is designed. Then, taking the BCU speed sensor's EMI event as mentioned before as an example, the validity and feasibility of the presented scheme are demonstrated, in which the waveform of the voltage signal reflecting measured speed and corresponding speed recognition result are used for verification. Then, the scheme's application study is further performed and the correctness of the BCU speed sensor measurement under multiple specific conditions regarding different TB contact conditions or different train speeds is evaluated in Section IV. Conclusions are drawn in Section V.

II. DEDUCTION FOR THE RELATION BETWEEN TRAIN BODY VOLTAGE AND BCU SPEED MEASUREMENT

According to the CRH380CL-type train, the closure of the door is controlled by the door control unit (DCU). When the measured speed in the DCU is more than 5 km/h, the door will refuse to open. Looking at both Fig. 3 and the corresponding meanings of the symbols given in Table I, because $u_D(t)$ is the only voltage signal that is sent into the DCU for identification, the final speed measurement result is decided by $u_D(t)$. In addition, as described in Fig. 3, $u(t)$ and $u_D(t)$

This article has been accepted for inclusion in a future issue of this journal. Content is final as presented, with the exception of pagination.
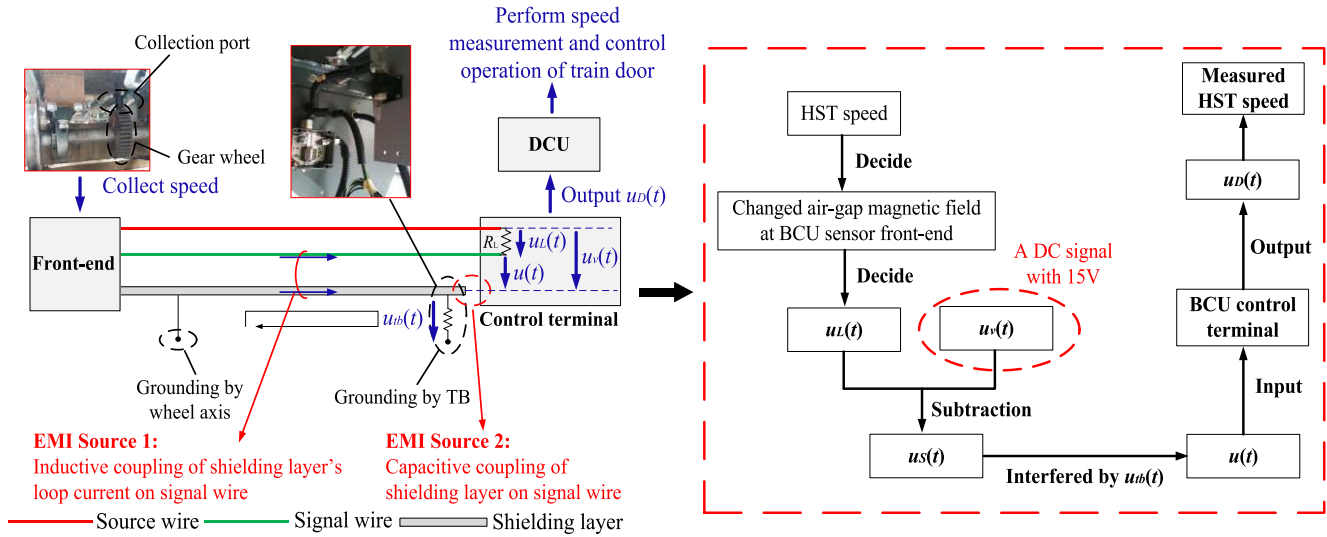
HUANG *et al.*: EVALUATION SCHEME FOR EMI

3

Fig. 3.   Equivalent circuit of BCU speed sensor in CRH380CL-type train and the corresponding speed measurement process.

are the input and output of the BCU speed sensor's control terminal, respectively. Fig. 3 also depicts the formation of $u(t)$. A Hall-effect current sensor is adopted in the BCU speed sensor. When the train speed is 0 km/h, the gear wheel at the train's wheel axis keeps static, and the air-gap magnetic field at BCU sensor's front-end remains unchanged resulting in $u_L(t)$ being 0 V. When the HST runs, the gear wheel is running along with train's wheel axis, and the air-gap magnetic field at BCU sensor's front-end constantly changes, causing $u_L(t)$ to alternately reach 0.7 and 1.4 V, i.e., presenting rectangular wave. Then, by performing a subtraction between $u_L(t)$ and $u_v(t)$ ($u_v(t)$ is a dc signal with 15 V), the $u_S(t)$, namely ideal $u(t)$, is obtained and input to the BCU speed sensor's control terminal. However, it is unavoidable that the input $u(t)$ is interfered by $u_{tb}(t)$. So, the output $u_D(t)$ and the corresponding speed measurement result may be influenced.

Combined with Fig. 3, for the BCU speed sensor, its front-end and control terminal are located at the axis (namely wheel axis) and the central position of TB, respectively. They are connected by transmission wire, which is mainly composed of source wire, signal wire and shielding layer. According to Fig. 3, $u_{tb}(t)$ may interfere $u(t)$ through two-coupling ways: inductive coupling of the shielding layer's loop current on signal wire and capacitive coupling of the shielding layer on signal wire. On this basis, it is assumed that the interference voltage $u_n(t)$ consists of $u_{n1}(t)$ and $u_{n2}(t)$. If the two EMI sources are reflected in an equation representing the relation between $u_{tb}(t)$ and $u(t)$, the $u_D(t)$ with the TB voltage fluctuation's impact can be obtained and the correctness of measured speed that has been interfered will be judged once we obtain TB voltage.

A. EMI 1: Inductive Coupling of $u_{tb}(t)$ on Signal Wire

For the shielding layer as shown in Fig. 3, one-end is connected to axis at front-end and the other is connected to TB at control terminal. Since the TB is under equal potential with the shielding layer at control terminal while the axis is

under equal potential with the shielding layer at frond-end, the loop currents [$i_{\text{loop}}(t)$] will be generated between the two grounding points because potential difference exists between the central position of TB and the axis where the front-end of BCU speed sensor is located. This potential difference is i.e., $u_{tb}(t)$, and it causes $i_{\text{loop}}(t)$.

The $i_{\text{loop}}(t)$ may generate coupling on signal wire due to the mutual inductive coupling of shielding layer's loop circuit on signal wire [17]. For the shielding layer, it is a network structure woven by dense copper wires. If the diameter of each copper wire d_x is smaller than the penetration depth of copper δ, the coupling of $i_{\text{loop}}(t)$ on signal wire will not be influenced [18], [19]. Hence, it is necessary to judge whether the $d_x < \delta$. Through measurement with vernier caliper, the d_x for each copper wire in shielding layer is obtained as around 1 mm. The δ is calculated by

$$\delta = \frac{1}{\sqrt{\pi f \mu \sigma}} \tag{1}$$

where f, μ and σ are frequency, permeability and conductivity, respectively. $\mu = 4\pi \times 10^{-7}$ H/m and $\sigma = 5.8 \times 10^7$ S/m for copper material.

For the voltages and currents of HST without considering high-frequency surge condition, the main frequency component is power-frequency, and the harmonic component is mainly gathered at the harmonic orders of third, fifth, seventh, and nineth. It is almost impossible for the highest harmonic order to be higher than 40th [20], [21]. Considering that the higher f leads to the smaller δ in (1), the 40th harmonic order, i.e., $f = 2000$ Hz, is selected as the highest harmonic order to obtain the smallest δ. The δ when $f = 2000$ Hz is calculated as 1.5 mm, which is larger than d_x. Therefore, since the smallest δ is larger than d_x, the coupling of $i_{\text{loop}}(t)$ on signal wire will not be influenced.

According to Fig. 4, R_S and M_S denote the shielding layer's resistance and the mutual-inductance between shielding layer and signal wire, respectively. The $u_{n1}(t)$, induced by $u_{tb}(t)$,
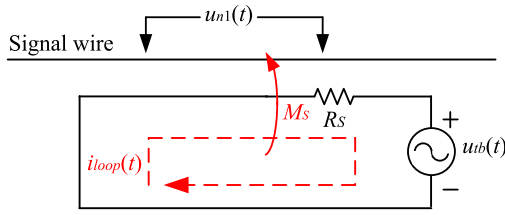
Fig. 4. Equivalent circuit for the formation of $i_{\text{loop}}(t)$.

is

$$u_{n1}(t) = M_s \frac{di_{\text{loop}}(t)}{dt}. \tag{2}$$

For the loop circuit of $i_{\text{loop}}(t)$

$$u_{\text{tb}}(t) = L_s \frac{di_{\text{loop}}(t)}{dt} + R_s i_{\text{loop}}(t) \tag{3}$$

where L_S denotes the self-inductance of the shielding layer.

By performing the Laplace transform for (2), (3), $u_{\text{tb}}(t)$ and $i_{\text{loop}}(t)$ are expressed as

$$\begin{cases} u_{n1}(\omega) = j\omega M_S i_{\text{loop}}(\omega) \\ i_{\text{loop}}(\omega) = \dfrac{u_{\text{tb}}(\omega)}{j\omega L_S + R_S} \end{cases} \tag{4}$$

where ω is the angular frequency. $u_{\text{tb}}(\omega)$ and $i_{\text{loop}}(\omega)$ are time-frequency conversion results aimed at $u_{\text{tb}}(t)$ and $i_{\text{loop}}(t)$. It is expressed as $u_{\text{tb}}(\omega) = L[u_{\text{tb}}(t)]$ and $i_{\text{loop}}(\omega) = L[i_{\text{loop}}(t)]$.

For the shielding layer, the whole magnetic flux $\Phi_1(t)$ generated by the $i_{\text{loop}}(t)$ will surround the signal wire, and L_S is

$$L_s = \frac{\Phi_1(t)}{i_{\text{loop}}(t)}. \tag{5}$$

The mutual inductance caused by the $i_{\text{loop}}(t)$ on the signal wire M_S is expressed as

$$M_s = \frac{\Phi_2(t)}{i_{\text{loop}}(t)} \tag{6}$$

where $\Phi_2(t)$ denotes the flux linkage caused by $i_{\text{loop}}(t)$ and signal wire.

Since the signal wire is surrounded by a shielding layer and their axes are nearly overlapped, the whole magnetic flux generated by the $i_{\text{loop}}(t)$ will nearly entirely surround the signal wire, namely $\Phi_1 = \Phi_2$ [22]. Thus $L_S = M_S$.

By combining (2)–(6), the equation reflecting the relation between $u_{n1}(t)$ and $u_{\text{tb}}(t)$ is formulated as

$$u_{n1}(\omega) = \left(\frac{j\omega}{j\omega + \frac{R_S}{M_S}} \right) u_{\text{tb}}(\omega) = \sum_{i=1}^{n} \left(\frac{j \cdot 2\pi f_1 \cdot i}{j \cdot 2\pi f_1 \cdot i + \frac{R_S}{L_S}} \right) \\ \times u_{\text{tb}}(2\pi f_1 \cdot i) \tag{7}$$

where f_1 denotes the power-frequency, $\omega = 2\pi f_1 \cdot i$ ($i = 1, 2, \ldots, n$).

B. EMI 2: Capacitive Coupling of $u_{tb}(t)$ on Signal Wire

In Fig. 5, a gap exists between the transmission wire's shielding layer and the control terminal of the BCU speed sensor. The electric field $[E_{\text{tb}}(t)]$ will be generated by $u_{\text{tb}}(t)$,
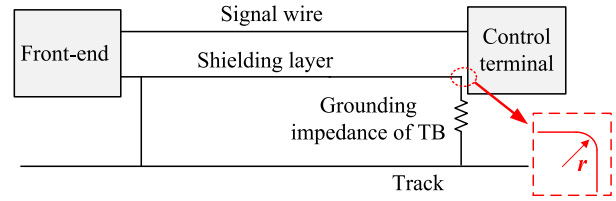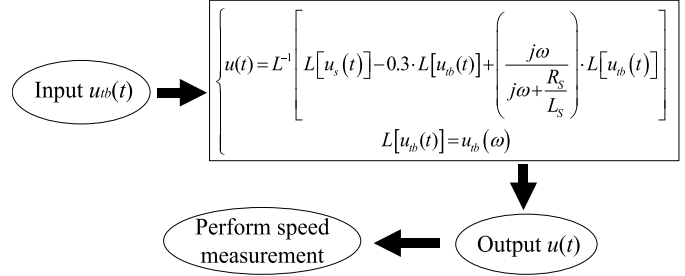

Fig. 5. Diagram of point effect.

Fig. 6. Implementation of BCU speed measurement evaluation scheme.

and the relation between them is seen in (8). It is obvious that the smaller cutting-edge radius r will lead to the larger $E_{\text{tb}}(t)$. As the r is the minimum, the $E_{\text{tb}}(t)$ caused by $u_{\text{tb}}(t)$ will reach a maximal, which is called as point effect [23]

$$E_{\text{tb}} = \frac{u_{\text{tb}}}{r}. \tag{8}$$

At the gap, the minimum cutting-edge radius of shielding layer, namely r_0, is 0.01 m. Meanwhile, the distance between source wire and signal wire, namely l_0, is 0.003 m. Therefore, the induced voltage between signal wire and source wire $u_{n2}(t)$ is described by:

$$u_{n2}(t) = \frac{l_0}{r_0} u_{\text{tb}}(t) = 0.3 u_{\text{tb}}(t) \tag{9}$$

Hence, by integrating (7) and (9), an equation reflecting the relation between $u(t)$ and $u_{\text{tb}}(t)$ is established as

$$\begin{cases} u(t) = L^{-1} \left[L[u_s(t)] - \left(\dfrac{j\omega}{j\omega + \frac{R_S}{L_S}} \right) L[u_{\text{tb}}(t)] \right. \\ \qquad\qquad \left. + 0.3 L[u_{\text{tb}}(t)] \right] \\ L[u_{\text{tb}}(t)] = u_{\text{tb}}(\omega). \end{cases} \tag{10}$$

III. DESIGN OF THE EVALUATION SCHEME

On the basis of (10), the realization of an evaluation scheme aimed at the TB voltage fluctuation's EMI influence on the BCU speed sensor's speed measurement is elaborated upon and is depicted in Fig. 6. It consists of three steps: 1) the input of $u_{\text{tb}}(t)$ into (10); 2) the output of $u(t)$ from (10); and 3) the measured speed's extraction from the waveform of output $u(t)$. The correctness of the speed measurement will finally be evaluated according to the actual train speed, which is also reflected in (10). If the measurement results are evaluated to be wrong, it can be concluded that the TB voltage fluctuation has influenced the train's operation, and it is necessary to
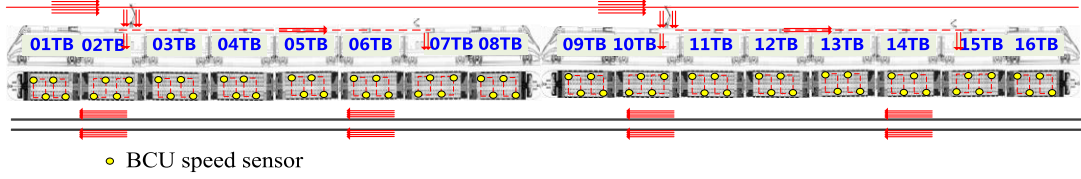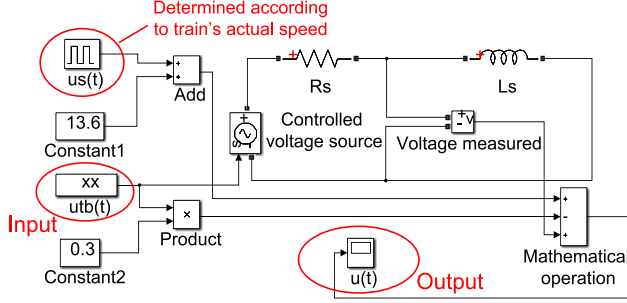
This article has been accepted for inclusion in a future issue of this journal. Content is final as presented, with the exception of pagination.

HUANG *et al.*: EVALUATION SCHEME FOR EMI

5

Fig. 7. Diagram of BCU sensor position distribution in CRH380CL-type train.

Fig. 8. Simulation model aimed at obtaining $u(t)$ based on $u_{\mathrm{tb}}(t)$.

take measures aimed at TB voltage, such as optimizing train's grounding system by replacing conventional earth resistor with SiC earth resistor to weaken TB voltage fluctuation [12].

A. Obtaining $u_{tb}(t)$

Fig. 7 depicts the BCU speed sensor distribution in the CRH380CL-type train. This train consists of 16 marshalling TBs with serial numbers from 01 to 16 for this paper. The BCU speed sensor's front-end is distributed at each axis of each TB and the control terminal is at the central section of their corresponding TBs. Combined with (10) and distribution of the BCU speed sensor, if $u_{\mathrm{tb}}(t)$ at the each TB is obtained, $u(t)$ of all the sensors can be calculated. So, the precondition of calculating correct $u(t)$ is that the $u_{\mathrm{tb}}(t)$ must be close to reality. The $u_{\mathrm{tb}}(t)$ can be measured, simulated or calculated by other means.

B. Obtaining $u(t)$ by Simulation

Regarding $u_{\mathrm{tb}}(t)$, it contains many harmonic components. According to (10), in order to obtain $u(t)$ on the premise of having $u_{\mathrm{tb}}(t)$, it is necessary to perform three steps: 1) extract the voltage component at each frequency of $u_{\mathrm{tb}}(t)$; 2) substitute the voltage component at each frequency of $u_{\mathrm{tb}}(t)$ into (10) to obtain the corresponding component of $u(t)$; and 3) integrate the voltages at each frequency of $u(t)$ to get the complete $u(t)$. However, it is difficult and error-prone to realize. Thus, a MATLAB/simulink simulation model based on (10) is set up to obtain $u(t)$ as illustrated in Fig. 8.

In Fig. 8, the output of model is $u(t)$, and the input excitation source of model has not only $u_{\mathrm{tb}}(t)$, but also $u_S(t)$. Regarding $u_S(t)$, it denotes the voltage signal that should be presented when sent into the BCU control terminal at the actual train speed v. The waveform of $u_S(t)$ is set solely on the basis of v. As known in Section II, the $u_S(t)$ is a subtraction result between $u_v(t)$ and $u_L(t)$. That is, $u_S(t) = 15 - u_L(t)$ because the $u_v(t)$ is a source signal of 15 V. When the train

is static, the $u_L(t) = 0$ V and the $u_S(t)$ is a dc signal of 15 V; when the train is running, due to the constantly changing air-gap magnetic field at BCU sensor's front-end, the caused $u_L(t)$ alternately reaches 0.7 and 1.4 V, and the $u_S(t)$ presents rectangular waves with high level of 14.3 V and low level of 13.6 V. In speed measurement, the cycle period of $u_S(t)$ (T) is read by the time quantum between two switch points from low level to high level. Meanwhile, the T is caused by the rotation rate n of the gear wheel in the BCU speed sensor's frond-end. If the HST speed is assumed to be v, (11) can be derived by integrating $2\pi r_z n = v/3.6$ and $n = 1/(CT)$

$$T = \frac{7.2\pi r_z}{Cv} = \frac{k}{v} \tag{11}$$

where r_z is the radius of gear wheel, C is the total number of gear wheel's sawteeth and $k = 7.2\pi r_z/C$.

Besides, there is still the first pulse of $u_S(t)$ to be determined when simulating $u_S(t)$. At the moment when the gear wheel begins to run along with train's wheel axis, the collection port as seen in Fig. 3 may be faced with gear wheel's tooth or gear wheel's groove. So, the first impulse of $u_S(t)$ may be a high level or a low level. However, according to (11), the speed measurement result relies on the T, but not the levels presented in the first impulse of $u_S(t)$. Moreover, the relation between n and v is $n = v/(7.2\pi r_z)$. Because, r_z is a very small value, the gear wheel rotates very quickly even if the train speed is slow. So, the level presented in the first impulse of $u_S(t)$ will hardly generate any influence on the train's speed measurement. Considering these, the initial level of $u_S(t)$ is set as high level for all the simulations in this paper.

To sum up, according to (11), the actual v value is considered in simulating the $u_S(t)$ in (10), which is reflected as an input excitation source in the model of Fig. 8.

Considering that the skin effect presented in the copper conductor under low-frequency electrical condition is almost nonexistent, the R_S and L_S in (10)/Fig. 8 are described as

$$
\begin{cases}
R_S = \rho \dfrac{l}{\pi\left(r_2^2 - r_1^2\right)} \\
L_S = \dfrac{\mu l}{2\pi}\left(\left(\dfrac{r_2^2}{r_2^2 - r_1^2}\right)^2 \ln\dfrac{r_2}{r_1} - \dfrac{r_2^2}{r_2^2 - r_1^2} + \dfrac{1}{4}\dfrac{r_2^2 + r_1^2}{r_2^2 - r_1^2} + \ln\dfrac{h}{r_2}\right)
\end{cases} \tag{12}
$$

where h denotes the distance between the rail and axis of shielding layer, r_1 and r_2 represent the inner radius and outer radius of shielding layer, respectively, ρ denotes the resistivity of shielding layer, i.e., $1.72 \times 10^{-8}\Omega \cdot$ m, μ denotes the permeability of shielding layer, i.e., $4\pi \times 10^{-7}$ H/m, and l denotes the length between the BCU speed sensor's front-end and control terminal.
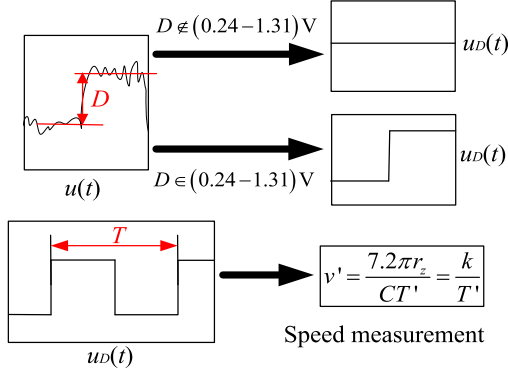
Fig. 9.   Diagram of conversion principle from $u(t)$ to $u_D(t)$.

C. Performing Evaluation for Speed Measurement by $u(t)$

As for the output $u(t)$, it will be converted into $u_D(t)$ for the final speed measurement. As described in Fig. 3, $u(t)$ and $u_D(t)$ are the input and the output of the BCU speed sensor's control terminal, respectively. After the conversion from $u(t)$ to $u_D(t)$, the $u_D(t)$ must be a smooth dc signal with 15 V or a rectangular wave that is only composed of high level and low level when HST is stationary or while running. Actually, when $u(t) = u_S(t)$, i.e., when $u(t)$ is without any interference, the output $u_D(t) = u(t)$. When $u(t) \neq u_S(t)$ but $u(t)$ presents an approximately rectangular waveform, namely consisting of alternating, sustained oscillating high voltages and low voltages, the output $u_D(t)$ is related to the difference between the averages of the high-voltage components and the low voltage components in $u(t)$, indicated by D' in this paper. As seen in Fig. 9, if D' is between the range of 0.24–1.31 V, a switch between high level and low level in $u_D(t)$ will occur; if D is beyond the range of 0.24–1.31 V, the level in $u_D(t)$ will remain unchanged. When $u(t)$ is not a rectangular wave, the $u_D(t)$ is output as a dc signal. Later, the cycle period of $u_D(t)$ (T') is recorded and the measured HST speed (v') is then obtained based on (11).

Comparing v' with v, the correctness of speed measurement can be determined. In terms of the door-controlling system, its manipulation is decided by DCU. If $v' < 5$ km/h is measured, the DCU will consider that the train is static and will not send instruction of closing door. If 5 km/h $< v' <$ 10 km/h is measured, the DCU will consider that the train is running and will send instruction of closing door. So, if v' does not conform with v, it illustrates that the $u_{tb}(t)$ has led to a faulty measurement of the train speed, and may cause the incorrect operation of door.

IV. VERIFICATION OF EVALUATION SCHEME

With the typical EMI fault occurring on the CRH380CL-type train's BCU speed sensor as Fig. 1 depicts, the validity and feasibility of the presented evaluation scheme is proven by combining an experiment performed at the Chinese Nanjing electric multiple unit station. Similar to the Chinese Wu-Xi railway station, the Nanjing station is also along the railway line from the Chinese Beijing to the Chinese Shanghai. Their station constructions are the same. All the experimental

conditions are set absolutely the same as the on-site conditions during the EMI event mentioned in Section I.

Fig. 10 illustrates the validation diagram for the proposed evaluation scheme (notice that $i_1(t)$, $i_2(t)$, $i_3(t)$, $i_4(t)$, $i_5(t)$, $i_6(t)$, $i_7(t)$, and $i_8(t)$ denote the operation grounding currents of the CRH380CL-type train and they are at 2-axis and 4-axis of 02TB, 07TB, 11TB, and 15TB in Fig. 11.).

As seen in Fig. 10, the signal seen in Fig. 1 [$u(t)$] is a voltage signal sent into the BCU control terminal from the front-end at the 4-axis of 10 TB. In experiment, this voltage signal sent from 4-axis of 10 TB and $i_1(t)$ to $i_8(t)$ are all measured. Meanwhile, measurement conditions are set equal to the conditions in Fig. 1. The measured voltage signal sent into BCU control terminal from 4-axis of 10 TB is the same as in Fig. 1, and is also marked as $u(t)$ here. The measured $i_1(t)$ to $i_8(t)$ are input into an electromagnetic transients program (EMTP) model to get the TB voltage at 4-axis of 10 TB ($u_{tb}(t)'$), which are the input of model shown in Fig. 8. The simulated voltage signal at 4-axis of 10 TB ($u(t)'$) is the model output, and is compared with the measurement result. The consistency of $u(t)'$ and $u(t)$, and measured speed and simulated speed will prove the correctness of the presented evaluation scheme.

The fast Fourier transform results of $i_1(t)$ to $i_8(t)$ are shown in Fig. 12, where I on the vertical axis is the effective value. In Fig. 12, the currents are mainly concentrated in power-frequency and harmonic orders of third, fifth, seventh, and ninth. So the power-frequency and harmonic orders of third, fifth, seventh and ninth are considered, and the expressions of $i_1(t)$ to $i_8(t)$ are set as in (13). Table II describes the corresponding amplitude and phase angle of each harmonic order current.

Then, for the CRH380CL-type train, $u_{tb}(t)'$ is simulated by an EMTP simulation model and the $i_1(t)$ to $i_8(t)$ are input as external excitation sources for this model in Fig. 13. Notice that the experimental position is at the catenary terminal, where the rail currents return back to the traction substation in a single direction. In HST, the traction currents flow into the rail by the HST's operation grounding system. Rail currents may enter TB through the TB grounding system, and the $u_{tb}(t)'$ are basically influenced by TB, train's grounding system and track. Combined with the actual TB electrical structure of HST, the EMTP model is composed of TB modules, grounding system modules and track modules. Based on the locations of the grounding axes, the module for each TB is divided into several modules. Their series connection is implemented, which is the same as in the rail module. Their modules consist of resistance and inductance. The impedance parameters of each module are decided by the axis distribution of TB (illustrated in Fig. 14) and unit-length parameters of the TB and the rail

$$i_i(t) = \sqrt{2}[a_i \cdot \cos(100\pi \cdot t + \alpha_i) + b_i \cdot \cos(300\pi \cdot t + \beta_i)$$
$$+ c_i \cdot \cos(500\pi \cdot t + \theta_i) + d_i \cdot \cos(700\pi \cdot t + \gamma_i)$$
$$+ e_i \cdot \cos(900\pi \cdot t + \lambda_i)] \quad (i = 1, 2, \ldots, 8). \quad (13)$$

For the TB resistance of CRH380CL-type train, it is measured by a MOH700 instrument and the measured resistance

This article has been accepted for inclusion in a future issue of this journal. Content is final as presented, with the exception of pagination.
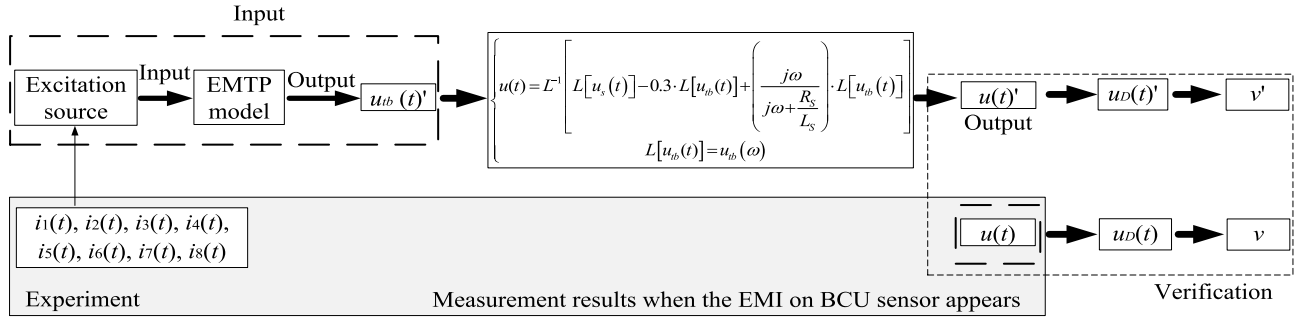
HUANG *et al.*: EVALUATION SCHEME FOR EMI

7

Fig. 10.   Validation diagram for the evaluation scheme for train body voltage's EMI impacts on speed measurement.

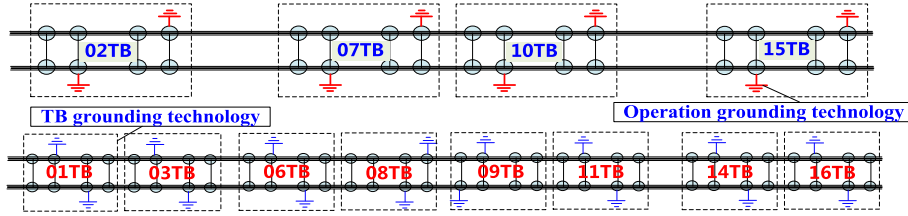Fig. 11.   Diagram of grounding system in CRH380CL-type train.

TABLE II

COEFFICIENT OF (13)

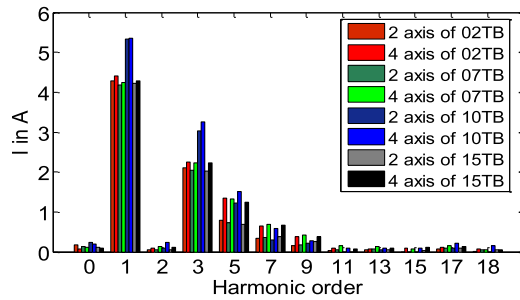| i	a_i	b_i	c_i	d_i	e_i	α_i	β_i	θ_i	γ_i	λ_i
1	4.28	2.10	0.80	0.33	0.15	$175°$	$183°$	$177°$	$0°$	$30°$
2	4.40	2.25	1.35	0.65	0.39	$178°$	$184°$	$181°$	$-4°$	$30°$
3	4.18	2.04	0.73	0.35	0.18	$181°$	$179°$	$194°$	$7°$	$40°$
4	4.25	2.23	1.33	0.68	0.42	$184°$	$185°$	$162°$	$-9°$	$-50°$
5	5.34	3.03	1.22	0.3	0.21	$155°$	$165°$	$190°$	$-20°$	$-50°$
6	5.35	3.26	1.51	0.58	0.28	$145°$	$165°$	$180°$	$30°$	$60°$
7	4.23	2.02	0.68	0.39	0.25	$185°$	$245°$	$183°$	$0°$	$40°$
8	4.28	2.23	1.24	0.67	0.38	$179°$	$230°$	$189°$	$-3°$	$10°$

Fig. 12.   Operation grounding currents for various harmonic orders.

for each TB is 0.4 mΩ. For the TB inductance, it is gained by (14) [24]

$$L_1 = \frac{\mu}{\pi} \ln \left(\frac{1}{4} + \frac{d_1}{r_4} \right) \qquad (14)$$

where L_1 represents the unit-length inductance of TB; μ denotes the permeability of TB, i.e., $4\pi \times 10^{-7}$ H/m; d_1 is the distance between TB conductor and P65-type rail; and r_4 equals the equivalent rail radius. In actuality, $d_1 = 0.883$ m and $r_4 = 0.176$ m. L_1 is obtained as 6.646×10^{-7} H/m.

For the connection resistance between adjacent TBs in the experiment, using the MOH700 instrument's measurement, the resistance between 10 and 11 TB is 100 mΩ, and the resistance between other adjacent TBs is 5.5 mΩ.

The TB grounding resistance is divided into carbon brush resistance and contact resistance between the wheel axis and the rail surface. Since one wheel axis bridges over two parallel rails and has only one carbon brush, the TB grounding resistance consists of one carbon brush resistance and half a contact resistance between one wheel and rail surface. For the former, it varies slightly with the HST speed; when the HST speed is 0 km/h, the measurement result by MOH700 instrument is 5.65 mΩ. Regarding the later, 0.4 mΩ is measured by MOH700 instrument. For the conditions in Fig. 1, each TB grounding resistance is obtained as 5.85 mΩ.

By performing on-site investigations at the Chinese Wu-Xi railway, it was found that the track insulator joint is located under the windshield between 09 and 10 TB for the CRH380CL-type train. Thus, it is necessary to determine the impedance parameters of the rail and track insulator joint. Studies about rail impedance parameters are abundant and the theoretical calculation is a general method. Some researches,
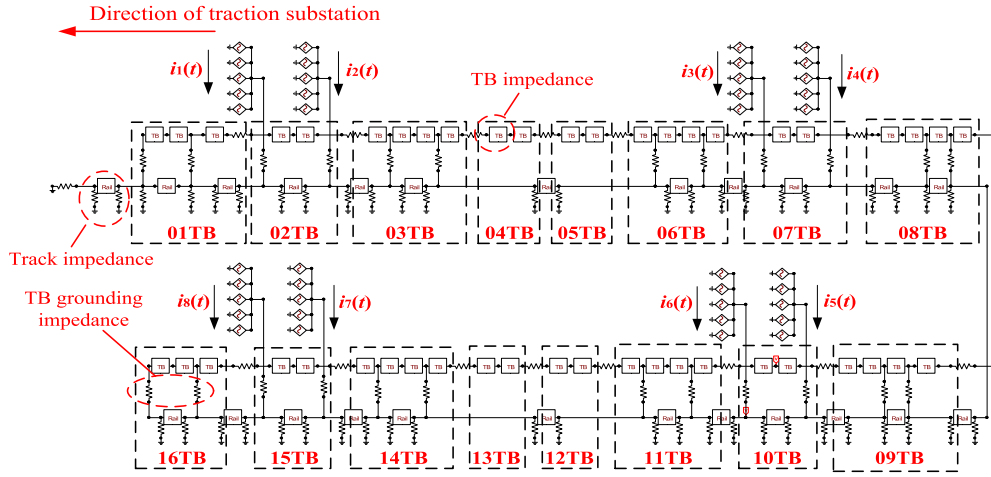
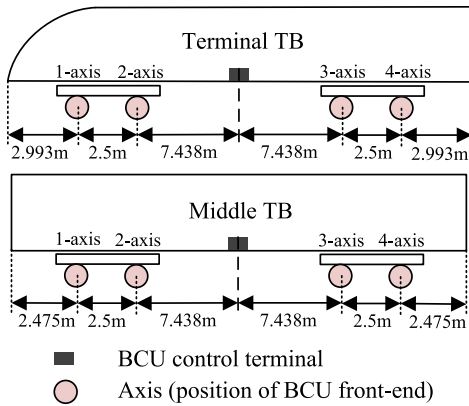Fig. 13.   EMTP simulation model regarding the calculations of $u_{\text{tb}}(t)'$ in CRH380CL-type train.

Fig. 14.   Distribution of axes in CRH380CL-type train.

Fig. 15.   Waveform of $u(t)'$.

such as in [25], improve on or correct existing methods. Some researches, such as in [26], focus on presenting a new approach. Besides, the simulation and experiment have also been widely combined (e.g., [27], [28]). Considering these, it is feasible to determine rail impedance parameters based on the aforementioned literature. The equivalent resistance and inductance are 0.135 mΩ/m and 3.560×10^{-6} H/m respectively for the P65-Type rail [29] used in experiment. Due to the excellent insulation performance between the rail and the ground, the leakage conductance is measured to be 0.01mS/m [30], [31]. For the track insulator joint resistance, the type of choke transformer is the BE2-F600, and the measurement result obtained by the MOH700 instrument is around 0.3 Ω–0.5 Ω. Combining [32], the insulator resistance is set to 0.33 Ω.

After simulation with the EMTP model, the $u_{\text{tb}}(t)'$ is gained and utilized as the input excitation source of simulation model in Fig. 8. Then, the R_S and L_S in Fig. 8 should be determined. For the L_S in (10), with measurements of vernier caliper, we obtain that $r_1 = 8$ mm and $r_2 = 10$ mm. Thus the unit-length L_S is 0.799 μH/m. Because the shielding layer uses copper material, it can be obtained that the unit-length R_S are 0.152 mΩ/m.
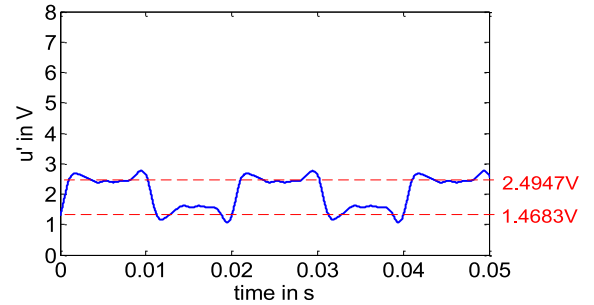
Furthermore, according to Fig. 14, the l is 9.938 m for the 1-axis and 4-axis of each TB and is 7.438 m for 2-axis and 3-axis of each TB. Since l is 9.938m for the sensor in the 4-axis of 10 TB, the R_S and L_S in Fig. 14 are 0.0015 Ω and 7.9405 μH, respectively. Then, using the model's simulation in Fig. 8, $u(t)'$ is obtained as seen in Fig. 15.

For (11), according to the BCU speed sensor in the CRH380CL-type HST, the total number of gear wheel's saw-teeth is $C = 80$ and the radius of the BCU speed sensor frond-end gear wheel is $r_z = 0.445$ m. Thus, k in (11) is 0.1258, and the relation between T and v is $T = 0.1258/v$

Based on Fig. 15, $u(t)'$ presents a periodic property with 0.02 s and high voltages and low voltages alternately occur for each 0.01 s. Furthermore, the average amplitudes of its alternating high voltages and low voltages are 2.4947 and 1.4684 V, respectively. The D' is 1.0263 V, which is in the identifying range of (0.24–1.31) V. So, the level state recorded in DCU will alter for 0.01s and the T' is 0.02 s. By substituting T' into $T = 0.1258/v$, the measured speed v' is 6.29 km/h, which nearly coincides with the measurement result, i.e., $v = 6.3$ km/h. Meanwhile, $u(t)'$ in Fig. 15 is similar to the measured waveform [$u(t)$] as seen in Fig. 1. Thus, the close similarity between the simulation results and experimental results validates the feasibility of the presented scheme, and also illustrates that the scheme is capable of evaluating the EMI aimed at BCU speed sensor under specific conditions.

This article has been accepted for inclusion in a future issue of this journal. Content is final as presented, with the exception of pagination.

HUANG *et al.*: EVALUATION SCHEME FOR EMI

9

TABLE III
MEASUREMENT RESULTS REGARDING CONTACT RESISTANCE BETWEEN
ADJACENT TBs UNDER FOUR CONDITIONS

| Screw condition	Contact resistance between adjacent TBs
Non-rusty and tightened	1.2-1.6 mΩ
Non-rusty and loosened	3.6-4.0 mΩ
Rusty and tightened	10.8-11.2 mΩ
Rusty and loosened	135.2-135.6 mΩ

Fig. 16. $u(t)'$ at each axis under different tightened contacts of adjacent TBs.

Fig. 17. $u(t)'$ at each axis under different loosened contacts of adjacent TBs.

V. ANALYSIS OF MULTIPLE SPECIFIC CONDITIONS BASED ON THE EVALUATION SCHEME

On the basis of proving the scheme's validity and feasibility, the scheme's application study is performed. As for the connection state between adjacent TBs, it is possible for nonrusty and tightened contact condition, rusty and tightened contact condition, nonrusty and loosened contact condition, and rusty and loosened contact condition to occur. With the MOH700 instrument, their resistance is measured in Table III.

For experimental verification in Section IV, the conditions are such that the HST speed is 0 km/h, the windshield between 09 and 10 TB is placed at track insulator joint, the contact resistance between 10 and 11 TB is 100 mΩ, and contact resistance between other adjacent TBs is 5.5 mΩ. According to Table III, taking four different TB connection conditions as examples, the correctness of speed measurement was analyzed using the scheme shown in Fig. 6. Since adjusting the TB contact resistance in model of Fig. 13 will change $u_{tb}(t)'$ and then affect $u(t)'$, in the first model application analysis, its operation condition is set that the TB contact resistances are respectively 1.4, 3.8, 11.0, and 135.4 mΩ, which correspond to four common TB contact states, on the premise of keeping other conditions consistent with verification of Section IV. For the reason that the train speed is low at most cases when passing insulator and in order to perform relative distinct and visual contrast for $u(t)'$, in the second model application analysis, the operational condition is set that the HST speed is 3.145 km/h under four common TB contact states while keeping other conditions consistent with the verification in Section IV.

A. Different TB Contacts When HST Is at 0 km/h

1) Tightened Connection Between Adjacent TBs: For the EMTP model in Fig. 13, because the train is static, the TB grounding resistance is set to 5.8 mΩ. Meanwhile, considering weather conditions, the tightened contact between adjacent TBs is divided into nonrusty condition and rusty condition, and 1.4 and 11.0 mΩ are set for simulating them, respectively. The other electrical parameters are completely consistent with the EMTP model in the verification of Section IV. For each TB, the l in (14) is the same for the 1-axis and 4-axis (9.9375 m), and the 2-axis and 3-axis (7.4375 m). So, $u(t)'$ at the 1-axis and the 2-axis of all TBs are only simulated because their results represent $u(t)'$ at all axes in the CRH380CL-type train.
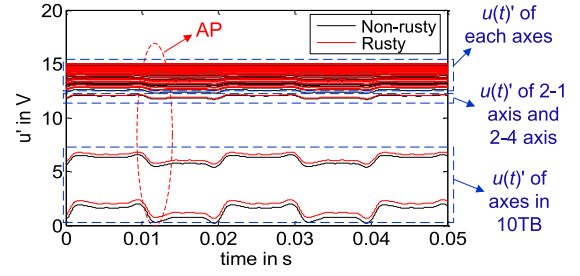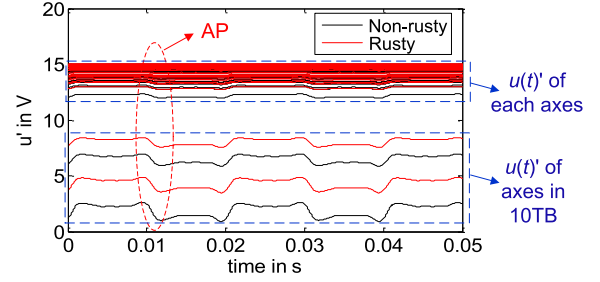
At the output port of the model in Fig. 8, Fig. 16 depicts the waveforms of $u(t)'$ at 1-axis and 2-axis of all the TBs under different tightened contact conditions of adjacent TBs. The $u(t)'$ without interference ($u_S(t)'$) is a DC signal with 15 V owing to $v = 0$ km/h. Therefore it is obvious that at most axes, $u_{tb}(t)'$ has a subtle effect on $u(t)'$. Also, for the 10 TB, track insulator joint exists under the windshield between 09 and 10 TB, which lets relatively more rail currents to enter 10 TB as described in Fig. 13. Thus the $u_{tb}(t)'$ of 10 TB is relatively higher and has a more obvious impact on $u(t)'$. Compared with non-rusty contact, the rusty contact will suppress the amount of rail currents flowing into TBs because of higher resistance (11 m Ω > 1.4 mΩ), which leads to lower $u_{tb}(t)'$ and lower interference. Thus, under rusty contact, $u(t)'$ at each axis is closer to $u_S(t)'$ compared with nonrusty contact.

2) Loosened Connection Between Adjacent TBs: Similarly, the loosened contact conditions of adjacent TBs are simulated. Combined with Table III, Fig. 17 shows the corresponding $u(t)'$. Similar to Fig. 16, $u_{tb}(t)'$ has a subtle effect on the $u(t)'$ nearly except for the axes of 10 TB. Because the contact resistance at rusty contact, i.e., 135.4 mΩ, is much larger than other three TB contact conditions, the hinder for rail current's flowing into TB is much stronger. The caused $u_{tb}(t)'$ is relative much lower, and it results in obviously lower interference, which coincides with the results of Fig. 17.

Integrating the $u(t)'$ of four TB contact states, Fig. 18 depicts the D' of all the TBs, where TB contact states 1–4 denote nonrusty and tightened contact, rusty and tightened contact, nonrusty and loosened contact, and rusty and loosened contact, respectively. The D' presents the highest at 10 TB in four contact conditions. Combining $T = 0.1258/v$ and transfer range of high level and low level in $u_D(t)'$ (0.24 V–1.31 V) from $u(t)'$, Table IV describes the

This article has been accepted for inclusion in a future issue of this journal. Content is final as presented, with the exception of pagination.

10

IEEE TRANSACTIONS ON INSTRUMENTATION AND MEASUREMENT

TABLE IV

SPEED MEASUREMENT EVALUATION RESULTS OF BCU SENSORS AT ALL AXES UNDER DIFFERENT TB CONTACT STATES WHEN HST IS AT 0 km/h

Axis	TB contact state				Axis	TB contact state				Axis	TB contact state				Axis	TB contact state			
	1	2	3	4		1	2	3	4		1	2	3	4		1	2	3	4
1-1, 1-4	√	√	√	√	1-2, 1-3	√	√	√	√	2-1, 2-4	×	√	√	√	2-2, 2-3	√	√	√	√
3-1, 3-4	√	√	√	√	3-2, 3-3	√	√	√	√	4-1, 4-4	√	√	√	√	4-2, 4-3	√	√	√	√
5-1, 5-4	√	√	√	√	5-2, 5-3	√	√	√	√	6-1, 6-4	√	√	√	√	6-2, 6-3	√	√	√	√
7-1, 7-4	√	√	√	√	7-2, 7-3	√	√	√	√	8-1, 8-4	√	√	√	√	8-2, 8-3	√	√	√	√
9-1, 9-4	√	√	√	√	9-2, 9-3	√	√	√	√	10-1, 10-4	×	×	×	×	10-2, 10-3	×	×	×	×
11-1, 11-4	√	√	√	√	11-2, 11-3	√	√	√	√	12-1, 12-4	√	√	√	√	12-2, 12-3	√	√	√	√
13-1, 13-4	√	√	√	√	13-2, 13-3	√	√	√	√	14-1, 14-4	√	√	√	√	14-2, 14-3	√	√	√	√
15-1, 15-4	√	√	√	√	15-2, 15-3	√	√	√	√	16-1, 16-4	√	√	√	√	16-2, 16-3	√	√	√	√

Fig. 18. D' of the $u(t)'$ at all axes under general four TB contact states.

Fig. 19. $u(t)'$ at each axis under different tightened contacts of adjacent TBs. (a) Adjacent TBs are at nonrusty contact. (b) Adjacent TBs are at rusty contact.

Fig. 20. $u(t)'$ at each axis under different loosened contacts of adjacent TBs. (a) Adjacent TBs are at nonrusty contact. (b) Adjacent TBs are at rusty contact.
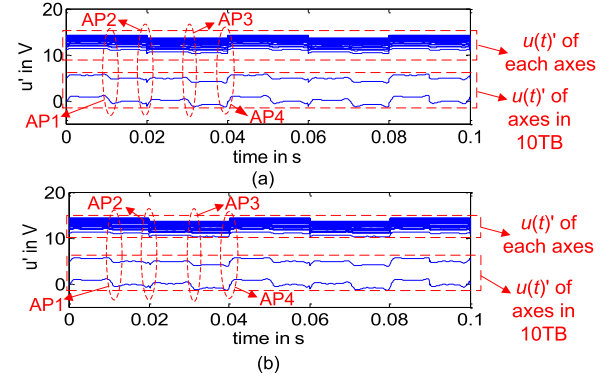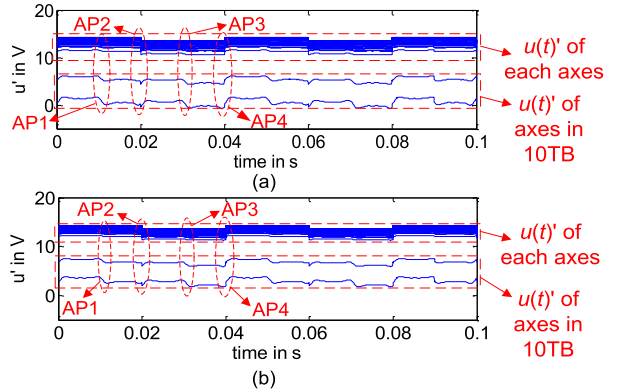
speed measurement results for all the axes. The BCU sensors at all axes of 10 TBs send error signal under TB contact state 2–4 while BCU sensors at axes of 2-1, 2-4 and all axes of 10 TBs send error signal under TB contact state 1. All of faulty results are the 6.290 km/h, which will result in the door's refusing to open.

B. Different TB Contacts When HST Is at 3.145 km/h

Based on the above four contact conditions between adjacent TBs, the $u(t)'$ is evaluated for HST's passing track insulator joint as the v is set to 3.145 km/h. Thus, the signal without interference ($u_S(t)'$) should be a rectangular wave with high level of 14.3 V and low level of 13.6 V. The corresponding period (T') is 0.04 s.

In the EMTP model used for obtaining $u_{tb}(t)'$, assuming that the HST speed is 3.145 km/h, the carbon brush resistance is measured as 5.75 mΩ and the TB grounding resistance is set to be 5.95 mΩ as the wheel-rail contact resistance is 0.2 mΩ. except that the TB contact impedance is set according to Table III, all the other electrical parameters are completely consistent with the EMTP model in the verification of Section IV.

Figs. 19 and 20 show the waveforms of $u(t)'$ at 1-axis and 2-axis of all the TBs under the four contact conditions. In Figs. 19 and 20, the $u(t)'$ presents a periodic property with 0.04 s. In each 0.04 s, the amplitudes of $u(t)'$ will change remarkably at around 0.01, 0.02, 0.03, and 0.04 s. So, in order to obtain the speed measurement results, it is necessary to judge whether the D' at each alternating point is in the range of (0.24–1.31) V. Combining Figs. 19 and 20, the $u(t)'$ at the four TB contact states are integrated, and their D' at 0.01, 0.02, 0.03, and 0.04 s are seen in Fig. 21(a)–(d). Because the track insulator

joint is under the windshield between 09 and 10 TB, the large insulator resistance will lead more rail currents to enter 10 TB by TB grounding system. Thus, the $u_{tb}(t)'$ at 10 TB presents relatively higher amplitudes and causes the most significant impact on $u(t)'$ at 10 TB, which agrees with Figs. 19 and 20.

Combined with Fig. 21(a)–(d), Table V depicts the final speed measurement results. The BCU sensors at the axis of 2-1, 2-4 and all the axes of 10 TBs send faulty signal under TB contact state 1; sensors at axis of 2-1, 2-4, 10-1, 10-4 send faulty signal under TB contact state 2; sensors at axis of 10-1 and 10-4 send error signal under TB contact
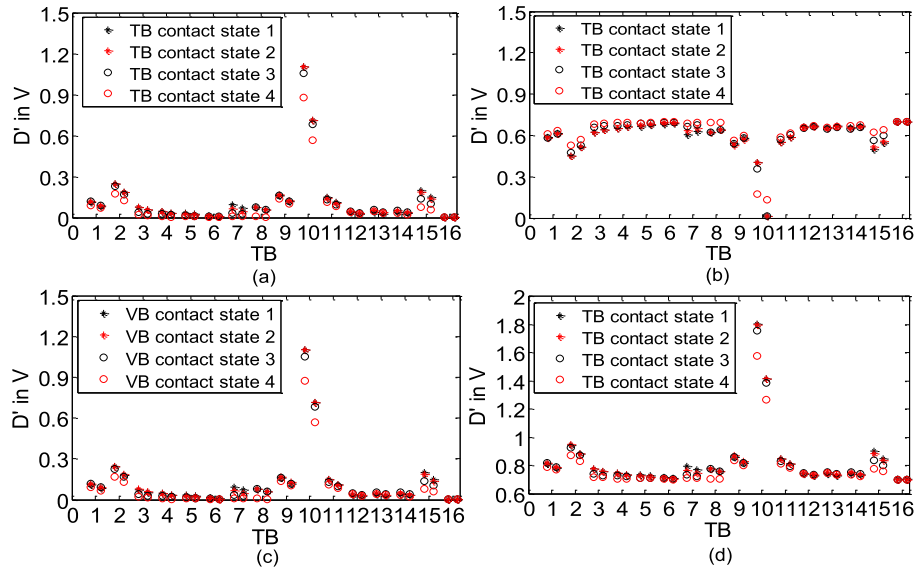
This article has been accepted for inclusion in a future issue of this journal. Content is final as presented, with the exception of pagination.

HUANG *et al.*: EVALUATION SCHEME FOR EMI   11

Fig. 21. D' of the $u(t)'$ at all axes in four alternating points. (a) AP 1 (at 0.01s). (b) AP 2 (at 0.02s). (c) AP 3 (at 0.03s). (d) AP 4 (at 0.04s).

TABLE V

SPEED MEASUREMENT EVALUATION RESULTS OF BCU SENSORS AT ALL AXES UNDER DIFFERENT TB CONTACT STATES WHEN HST IS AT 3.145 km/h

Axis	TB contact state				Axis	TB contact state				Axis	TB contact state				Axis	TB contact state			
	1	2	3	4		1	2	3	4		1	2	3	4		1	2	3	4
1-1, 1-4	√	√	√	√	1-2, 1-3	√	√	√	√	2-1, 2-4	×	×	√	√	2-2, 2-3	√	√	√	√
3-1, 3-4	√	√	√	√	3-2, 3-3	√	√	√	√	4-1, 4-4	√	√	√	√	4-2, 4-3	√	√	√	√
5-1, 5-4	√	√	√	√	5-2, 5-3	√	√	√	√	6-1, 6-4	√	√	√	√	6-2, 6-3	√	√	√	√
7-1, 7-4	√	√	√	√	7-2, 7-3	√	√	√	√	8-1, 8-4	√	√	√	√	8-2, 8-3	√	√	√	√
9-1, 9-4	√	√	√	√	9-2, 9-3	√	√	√	√	10-1, 10-4	×	×	×	√	10-2, 10-3	×	√	√	√
11-1, 11-4	√	√	√	√	11-2, 11-3	√	√	√	√	12-1, 12-4	√	√	√	√	12-2, 12-3	√	√	√	√
13-1, 13-4	√	√	√	√	13-2, 13-3	√	√	√	√	14-1, 14-4	√	√	√	√	14-2, 14-3	√	√	√	√
15-1, 15-4	√	√	√	√	15-2, 15-3	√	√	√	√	16-1, 16-4	√	√	√	√	16-2, 16-3	√	√	√	√

state 3; and no faulty signal is sent under TB contact state 4. The HST speed is falsely measured to be 6.290 km/h at axes of 2-1, 2-4 under TB contact state 1, 2, which causes the door to refuse to open when the door should open because actual train speed is 3.145 km/h.

VI. CONCLUSION

Focusing on the HST door's incorrect operation that is caused by faulty speed measurement of the BCU speed sensor, this paper proposes an evaluation scheme intended to analyze the TB voltage fluctuation's EMI influence on the BCU speed sensor's speed measurement. An experimental verification aimed at this scheme is performed based on a real event. Also, taking some specific conditions as example, application study of this scheme is implemented. In the scheme, the influence of the TB voltage fluctuation is reflected by a model representing the relation between TB voltages and voltage signal reflecting measured speed. The TB voltages and the voltage signal are the input and output of this model, respectively. Because the actual train speed is set as an inherent factor of the model, the measured speed with the EMI impact is ultimately determined by the model output. On this basis, the influence of TB voltage fluctuation on the speed measurement can be judged by comparing the model output and the actual speed.

This evaluation scheme can not only provides the opportunity to determine the correctness of speed measurement under the premise of collecting TB voltages, but also provides references for taking the timely measures to prevent faulty speed measurement such as weakening TB voltage fluctuations.

The evaluation scheme suggests further investigations on evaluating the influential factors of measured BCU speed signal, such as harmonic contents of TB voltages, material corrosion of sensor wire, etc. Also, a developing system of continuously collecting TB voltage fluctuation is necessary for real-time assessment of the correctness of the BCU speed measurement. This will help to put the evaluation scheme into actual engineering application, and improve reliability for safe protection in HST.

REFERENCES

[1] J. B. Yan, "Study on the electromagnetic compatibility of shaft end speed sensors in CRH3 electric multiple unit," M.S. thesis, Dept. Elect. Eng., Southwest Jiaotong Univ., Chengdu, China, 2015.

[2] A. Creosteanu and L. Creosteanu, "Investigation of the electromagnetic interference effect on the speed sensor of an aircraft starter generator," in *Proc. IEEE Int. Semiconductor Conf.*, Bologna, Italy, Oct. 2012, pp. 16–18.

[3] A. Creosteanu and L. Creosteanu, "Study on the electromagnetic susceptibility of the speed sensor of an aircraft starter generator," in *Proc. IEEE Int. Semiconductor Conf.*, Bologna, Italy, Sep. 2012, pp. 187–190.

[4] O. Aiello, P. Crovetti, and F. Fiori, "Investigation on the susceptibility of hall-effect current sensors to EMI," in *Proc. Int. Symp. Electromagn. Compat.*, Sep. 2011, pp. 368–372.

[5] S. Hussmann and P. A. Hu, "A microcomputer controlled ICPT power pick-up and its EMC considerations for moving sensor applications," in *Proc. Int. Conf. Power Syst. Technol.*, vol. 4. Oct. 2002, pp. 1011–1015.

[6] S. Dhia, A. Boyer, B. Vrignon, M. Deobarro, and T. V. Dinh, "On-chip noise sensor for integrated circuit susceptibility investigations," *IEEE Trans. Instrum. Meas.*, vol. 61, no. 3, pp. 696–707, Mar. 2012.

[7] C. Spindler, "New EMC-testing-method for smart sensors during for IC-design-process," in *Proc. Int. Symp. Electromagn. Compat.*, Gothenburg, Sweden, Sep. 2014, pp. 1186–1189.

[8] A. Masi, A. Danisi, R. Losito, and Y. Perriard, "Ironless position sensor with intrinsic immunity to external magnetic fields," in *Proc. IEEE Sensors*, Limerick, Ireland, Oct. 2011, pp. 2018–2021.

[9] A. Danisi, A. Masi, R. Losito, and Y. Perriard, "Electromagnetic analysis and validation of an ironless inductive position sensor," *IEEE Trans. Instrum. Meas.*, vol. 62, no. 5, pp. 1267–1275, May 2013.

[10] J. Yang, "EMC experiment and protection method on control vehicle speed and distance measuring equipment of CRH2 HST," *Railway Signaling Commun. Eng.*, vol. 7, no. 5, pp. 21–24, Oct. 2010.

[11] J. Yan, F. Zhu, J. Li, M. Sha, and D. Yuan, "Electromagnetic interference measurement and analysis of high-speed electric multiple units speed sensor," *J. Electron. Meas. Instrum.*, vol. 29, no. 3, pp. 433–438, Mar. 2015.

[12] S. Hatsukade, "Reduction method of surge voltage on AC railcar's body," *Quart. Rep. RTRI*, vol. 50, no. 2, pp. 70–75, May 2009.

[13] K. Huang, Z. G. Liu, and Y. Wang, "Analysis of vehicle body over-voltage under Ground's automatic electrical phase," in *Proc. Int. Conf. Inf. Sci. Technol.*, Changsha, China, Apr. 2015, pp. 260–264.

[14] S. Yang, B. J. Gao, G. Q. Gao, P. Chen, X. Huang, and Y. T. Wang, "Analysis of surge overvoltage of dropping pantograph for high-speed EMUs," *J. China Railway Soc.*, vol. 07, pp. 46–50, Jul. 2015.

[15] S. Xiao, Y. Wen, J. Zhang, and S. Chen, "Impedance characteristics of EMU MR-139 earthing resistor," *J. Beijing Jiaotong Univ.*, vol. 37, no. 6, pp. 39–44, Dec. 2013.

[16] W. F. Han *et al.*, "Analysis of railcar's body over-voltage for electric multiple unit in the case of lightning catenary," *J. Railway Sci. Eng.*, vol. 10, no. 4, pp. 117–123, Aug. 2013.

[17] B. Yi and Z. Z. Wang, "Parameters calculation of shield cable and crosstalk between shielding layer and core wires," *High Voltage Eng.*, vol. 34, no. 4, pp. 804–808, Apr. 2008.

[18] A. Editor and W. T. Smith, *Electromagnetics: Based on Schaum's Outline of Theory and Problems of Electromagnetics*, J. A. Edminister, Ed., 2nd ed. New York, NY, USA: McGraw-Hill, 2003, pp. 156–157.

[19] J. D. Jackson, *Classical Electrodynamics*. Hoboken, NJ, USA: Wiley, 1962, pp. 224–225.

[20] W. H. Chen, *Handbook of EMC*. Beijing, China: Machinery Industry Press, 1998, pp. 226–227.

[21] "National technical committee for standardization of radio interference," in *Implementation Guide of EMC Standards*. Beijing, China: China Standard Press, 2010, pp. 125–126.

[22] H. M. Lu, *Engineering Electromagnetic Compatibility*. Xi'an, China: Xidian Univ. Press, 2003, pp. 52–53.

[23] L. Enze, "The application of a surface charge density distribution function to the solution of boundary value problems," *J. Phys. D, Appl. Phys.*, vol. 20, no. 12, pp. 1609–1615, Dec. 1987.

[24] H. Wu, "Research on train body over-voltage surge," M.S. thesis, Dept. Elect. Syst. Control Inf. Syst., Southwest Jiaotong Univ., Chengdu, China, 2013.

[25] A. Mariscotti and P. Pozzobon, "Resistance and internal inductance of traction rails at power frequency: A survey," *IEEE Trans. Veh. Technol.*, vol. 53, no. 4, pp. 1069–1075, Jul. 2004.

[26] R. J. Hill and D. C. Carpenter, "Determination of rail internal impedance for electric railway traction system simulation," *IEE Proc. B-Electr. Power Appl.*, vol. 138, no. 6, pp. 311–321, Nov. 1991.

[27] A. Mariscotti and P. Pozzobon, "Measurement of the internal impedance of traction rails at audio frequency," *IEEE Trans. Instrum. Meas.*, vol. 53, no. 3, pp. 792–797, Jun. 2004.

[28] H. Nong and J. Lin, "Study on rail load measurement base on finite element analysis," in *Proc. Int. Conf. Electron. Meas. Instrum.*, Beijing, China, Aug. 2009, pp. 1-708–1-713.

[29] G. Wu *et al.*, "Study on the performance of integrated grounding line in high-speed railway," *IEEE Trans. Power Del.*, vol. 26, no. 3, pp. 1803–1810, Jul. 2011.

[30] G. Yang, M. G. Liu, N. Li, and Z. J. Qu, "Research on model of rail potential distribution and its simulation," *J. Beijing Jiaotong Univ.*, vol. 34, no. 2, pp. 137–141, Apr. 2010.

[31] "Engineering design and identification center of ministry of railways," in *Engineering Design Guide for Railway Integrated Grounding and Signal Equipment Lightning Protection System*. Beijing, China: Railway Press, 2009.

[32] (Mar. 25, 2015) *Xi'an Railway Substation Xi'an Electrical Equipment Factory. Instructions for BE1(2)-F-Type Choke Transformer [EB/OL]*. [Online]. Available: http://www.docin.com/p-627483172.html

Ke Huang (S'16) received the B.S. degree in electrical engineering from Southwest Jiaotong University, Chengdu, China, in 2013, where he is currently pursuing the Ph.D. degree in electrical engineering.

His current research interests include locomotive over-voltage and grounding technology, and reliability analysis on the pantograph-catenary electrical contact.

Zhigang Liu (M'06–SM'16) received the Ph.D. degree in power system and its automation from the Southwest Jiaotong University, Chengdu, China, in 2003.

He is currently a Full Professor with the School of Electrical Engineering, Southwest Jiaotong University. His current research interests include signal processing and its applications in power systems, and pantograph-catenary dynamic performance and arcing theory.

Feng Zhu received the Ph.D. degree in railway traction electrification and automation from the Southwest Jiaotong University, Chengdu, China, in 1997.

He is currently a Full Professor with the School of Electrical Engineering, Southwest Jiaotong University. His current research interests include locomotive over-voltage and grounding technology, electromagnetic theory and numerical analysis of electromagnetic field, and electromagnetic compatibility analysis and design.

Zongsheng Zheng received the B.S. degree in bioinformatics from Southwest Jiaotong University, Chengdu, China, in 2013, where he is currently pursuing the Ph.D. degree in electrical engineering.

His research interests include adaptive signal processing and its application in the electrified railway industry.

Ye Cheng received the B.S. degree in electrical engineering from Southwest Jiaotong University, Chengdu, China, in 2015, where she is currently pursuing the M.S. degree in electrical engineering.

Her current research interests include analysis on the suppression of catenary and locomotive over-voltage, and the optimization of locomotive grounding technology.